











Shapes of rotating normal fluid ^3He versus superfluid ^4He droplets in molecular beams

Deepak Verma ¹, Sean M. O. O'Connell ¹, Alexandra J. Feinberg ¹, Swetha Erukala ¹, Rico Mayro P. Tanyag ^{1,2}, Charles Bernardo,^{3,4} Weiwu Pang,⁵ Catherine A. Saladrigas,^{6,7} Benjamin W. Toulson,⁶ Mario Borgwardt ⁶, Niranjan Shivaram ^{8,9}, Ming-Fu Lin,⁸ Andre Al Haddad,¹⁰ Wolfgang Jäger ¹¹, Christoph Bostedt,^{10,12} Peter Walter,⁸ Oliver Gessner ^{6,*} and Andrey F. Vilesov ^{1,3,†}

¹*Department of Chemistry, University of Southern California, Los Angeles, California 90089, USA*

²*Institute for Optics and Atomic Physics, Technical University of Berlin, Berlin 10623, Germany*

³*Department of Physics and Astronomy, University of Southern California, Los Angeles, California 90089, USA*

⁴*School of Information Systems, BINUS University, Jalan K. H. Syahdan No. 9, Kemanggis, Palmerah, Jakarta 11480, Indonesia*

⁵*Viterbi School of Engineering, University of Southern California, Los Angeles, California 90089, USA*

⁶*Chemical Sciences Division, Lawrence Berkeley National Laboratory, Berkeley, California 94720, USA*

⁷*Department of Chemistry, University of California, Berkeley, California 94720, USA*

⁸*LCLS, SLAC National Accelerator Laboratory, 2575 Sand Hill Road, Menlo Park, California 94025, USA*

⁹*Department of Physics and Astronomy, Purdue University, West Lafayette, Indiana 47907, USA*

¹⁰*Laboratory for Femtochemistry (LSF), Paul Scherrer Institute, Forschungsstrasse 111, 5232 Villigen-PSI, Switzerland*

¹¹*Department of Chemistry, University of Alberta, Edmonton, Alberta T6G 2G2, Canada*

¹²*LUXS Laboratory for Ultrafast X-ray Sciences, Institute of Chemical Sciences and Engineering, École Polytechnique Fédérale de Lausanne (EPFL), CH-1015, Lausanne, Switzerland*



(Received 12 March 2020; revised 28 May 2020; accepted 28 May 2020; published 8 July 2020)

Previous single-pulse extreme ultraviolet and x-ray coherent diffraction studies revealed that superfluid ^4He droplets obtained in a free jet expansion acquire sizable angular momentum, resulting in significant centrifugal distortion. Similar experiments with normal fluid ^3He droplets may help elucidate the origin of the large degree of rotational excitation and highlight similarities and differences of dynamics in normal and superfluid droplets. Here, we present a comparison of the shapes of isolated ^3He and ^4He droplets following expansion of the corresponding fluids in vacuum at temperatures as low as ~ 2 K. Large ^3He and ^4He droplets with average radii of ~ 160 and ~ 350 nm, respectively, were produced. We find that the majority of the shapes of ^3He droplets in the beam correspond to rotating oblate spheroids, in agreement with previous observations for ^4He droplets. The aspect ratio of the droplets is related to the degree of their rotational excitation, which is discussed in terms of reduced angular momenta (Λ) and reduced angular velocities (Ω), the average values of which are found to be similar in both isotopes. This similarity suggests that comparable mechanisms induce rotation regardless of the isotope. We hypothesize that the observed distribution of droplet sizes and angular momenta originates from processes in the dense region close to the nozzle, where a significant velocity spread and frequent collisions between droplets induces excessive rotation followed by droplet fission.

DOI: [10.1103/PhysRevB.102.014504](https://doi.org/10.1103/PhysRevB.102.014504)

I. INTRODUCTION

Bosonic superfluid helium-4 (^4He) droplets, produced in molecular beams, constitute a versatile medium for experiments in physics and chemistry. Notably, droplets consisting of a few thousand He atoms are frequently used as ultracold matrices for the spectroscopic interrogation of single molecules, radicals, ionic species, and diverse clusters [1–6]. Single molecules embedded in ^4He droplets can also provide a unique probe for superfluidity on atomic-length scales via renormalization of molecular rotational constants [7–9]. More recently, experiments have been extended to much larger ^4He droplets, containing up to $\sim 10^{11}$ atoms, and ranging in diameter from hundreds of nanometers up to a few micrometers

[10]. Single droplets in this size range have been studied by ultrafast coherent scattering using femtosecond x-ray and XUV pulses from free electron lasers (FELs) and intense, laboratory-based high-order harmonic sources [11–17]. It was found that large ^4He droplets can have sizable angular momentum and can be subject to considerable centrifugal distortion [11,14–17]. Rotation of superfluid ^4He droplets is associated with the creation of quantum vortices, a physical manifestation of quantized angular momentum in the bosonic species [18–21]. Quantum vortices inside ^4He droplets have been visualized by doping them with a large number of xenon (Xe) atoms. The dopants are attracted to the vortices, inducing aggregation around the vortex cores and the formation of filament-shaped clusters [11–13,17].

Experiments involving droplets of the rare fermionic helium-3 isotope (^3He) have also been performed [7,22–30]. While ^3He may exist as a superfluid at temperatures below $T \approx 1$ mK [31,32], it is a normal fluid at typical molecular

*ogessner@lbl.gov

†vilesov@usc.edu

beam temperatures of ~ 0.15 K [29]. Recent density functional calculations show that the rotating ^3He droplets should follow corresponding classical shapes [33]. It is important to expand x-ray imaging experiments to rotating ^3He droplets to enable a direct comparison of droplet shapes and rotational properties of the two quantum fluids.

In this article, we report on the characterization of ^3He droplets produced with nozzle temperatures as low as ~ 2 K. Using ultrafast x-ray scattering at an FEL, the properties of individual, free ^3He and ^4He droplets are analyzed and their sizes, shapes, and angular momenta are compared. A wide range of ^3He and ^4He droplet sizes are obtained with average radii of 162 and 355 nm, respectively. An overwhelming majority of the droplets have pseudospheroidal shapes, characterized by the aspect ratio of the major and minor axes. From the aspect ratios, the reduced angular momenta and angular velocities are obtained using the corresponding stability diagram for classical viscous droplets [14,34,35]. The aspect ratios of droplets from both isotopes are found to have average values of 1.074 for ^3He and 1.088 for ^4He . Accordingly, the reduced angular momentum and reduced angular velocity in ^3He and ^4He droplets are similar. Comparison of the results obtained with ^4He and ^3He at different expansion conditions may help to gain a better understanding of the mechanism underlying the production of rotating droplets in free nozzle beam expansion sources.

II. EXPERIMENT

He droplets are produced by expanding pressurized He through a cryogenic nozzle with a $5\text{-}\mu\text{m}$ orifice into vacuum, the details of which are described elsewhere [1,4,5,10]. In vacuum, the temperature of the droplets further decreases via evaporative cooling down to 0.15 and 0.38 K for ^3He [29] and ^4He [7], respectively. Phase diagrams for ^3He and ^4He containing some typical expansion isentropes are presented in Sec. S1 of the Supplemental Material (SM) [36]. Considering the lower critical point of ^3He ($T_C = 3.3$ K, $P_C = 1.1$ atm) compared to that of ^4He ($T_C = 5.2$ K, $P_C = 2.3$ atm), lower nozzle temperatures are required to obtain ^3He droplets of similar size to of ^4He droplets. For example, for a nozzle stagnation pressure of $P_0 = 20$ bars, previous experiments demonstrate that ^4He droplets with an average number of atoms $\langle N_4 \rangle = 10^7$ are produced at a nozzle temperature of $T_0 = 7$ K, [10] while $T_0 = 5$ K is required to obtain ^3He droplets with the same average number of atoms $\langle N_3 \rangle = 10^7$ [25–27,37]. The temperature difference of 2 K in T_0 correlates well with the corresponding difference in critical temperatures of the two isotopes. Large ^4He droplets can be produced with modern closed-cycle refrigerators that can reach temperatures down to ~ 3.5 K. However, to reach the lower temperatures required to produce large ^3He droplets, we instead employed a liquid helium flow cryostat, the LT3 from Advanced Research Systems, with a cooling power of up to 1 W at 1.8 K. Droplets of ^3He and ^4He are produced at constant $P_0 = 20$ bars and varying T_0 , ranging from 2 to 4.5 K. The temperature was measured using a calibrated silicon diode (Lakeshore DT-670-CU) attached to the copper block close to the nozzle.

Due to the considerable cost of ^3He gas, a recycling system is employed during the experiments as described in

Sec. S2 of the SM [36]. Filling the system requires about 10 liter \times bar of room temperature ^3He . For comparison, at standard operating conditions ($T_0 = 3$ K, $P_0 = 20$ bars), the flow rate of the He gas is ~ 3 cm 3 bars/s and the filling amount of gas would only be sufficient for about 1 h of operation. During the experiments, ^3He gas is continuously collected from the exhausts of the backing scroll pumps, purified in a liquid nitrogen cooled zeolite trap, pressurized by a metal membrane compressor and resupplied to the nozzle with minimal losses. Any contaminants are constantly removed from the ^3He sample by the recycling system. The droplet source was stable over several days, indicating the purity of the ^3He remained high throughout the experiment. The ^3He gas used is 99.9% pure with the remaining 0.1% impurity being mostly ^4He . The residual ^4He will be mostly dissolved in the ^3He droplets, taking into account that its solubility is $\sim 0.1\%$ at 0.15 K [32]. Any possible pockets of a ^4He -rich phase in ^3He droplets are too small to give rise to any measurable effects in the diffraction patterns. Based on the rest gas pressure of less than 10^{-7} mbar and a beam path length from the nozzle to the interaction point of about 70 cm, the droplets will capture, on average, fewer than 500 rest gas particles (mostly water molecules), again too small a number to be detected in the diffraction experiments.

The experiments are performed using the LAMP end station at the atomic, molecular, and optical (AMO) instrument of the Linac Coherent Light Source (LCLS) FEL [38,39]. The focused FEL beam [~ 2 μm full width at half maximum (FWHM)] intersects the He droplet beam ~ 70 cm downstream from the nozzle. The FEL is operated at a pulse repetition rate of 120 Hz, a photon energy of 1.5 keV ($\lambda = 0.826$ nm), a pulse energy of ~ 1.5 mJ, and a pulse duration of ~ 100 fs (FWHM). The small pulse length and large number of photons per pulse ($\sim 10^{12}$) enable the instantaneous capture of the shapes of individual droplets. Diffraction images are recorded with a *pn*-charge-coupled device (*pn*CCD) detector containing 1024×1024 pixels, each 75×75 μm^2 in size, which is centered along the FEL beam axis ~ 735 mm downstream from the interaction point. The detector consists of two separate panels (1024×512 pixels each) located closely above and below the x-ray beam. Both panels also have a central, rectangular cutout to accommodate the primary x-ray beam. The diffraction patterns are recorded at small scattering angles and, thus, predominantly contain information on the column density of the droplets in the direction perpendicular to the detector plane.

III. RESULTS

Figure 1 shows several diffraction patterns from pure ^3He droplets. The images are characterized by sets of concentric contours. Images in Figs. 1(a) and 1(b) exhibit a series of circular and elliptical contours, respectively, with different spacings between their respective rings. Figure 1(c), however, shows an elongated diffraction contour with pronounced streaks radiating away from the center. These diffraction patterns are characteristic of spherical [Fig. 1(a)], and spheroidal (oblate) or capsule (prolate) [Figs. 1(b) and 1(c)] droplet shapes, as previously observed in ^4He droplets [11,14,16,17]. Spheroidal and prolate shapes result from centrifugal deformation of droplets with considerable angular momentum.

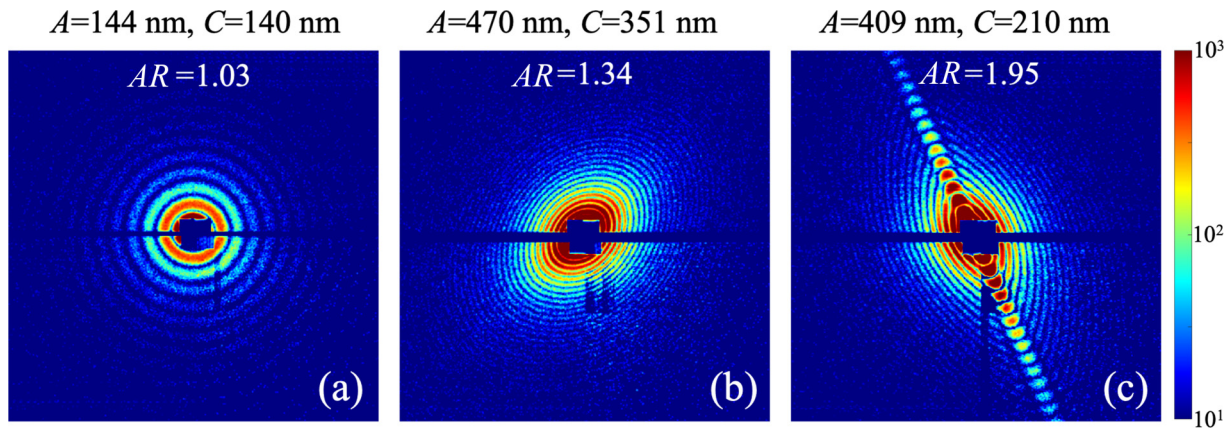


FIG. 1. Diffraction patterns of pure ^3He droplets shown on a logarithmic color scale as indicated on the right. Images represent the central 660×660 detector pixels. Corresponding droplet projection half axes (A , C) and their aspect ratio (AR) are displayed at the top of each image.

The droplet shapes are described by the distances between the center and the surface in three mutually perpendicular directions: $a \geq b \geq c$. For an oblate axisymmetric droplet, $a = b > c$, with c along the rotation axis, whereas $a > b > c$ in the case of triaxial prolate shapes with c along the rotation axis [11,14]. The observed diffraction patterns do not provide direct access to the actual values of a , b , and c , due to the droplets' unknown orientations with respect to the x-ray beam. Instead, the images are characterized by the two half axes of the projection of a droplet onto the detector plane, which will be referred to as A and C ($A > C$), corresponding to a projection aspect ratio, $AR = A/C$. For an axisymmetric oblate droplet having an unknown orientation with respect to the x-ray beam, the value of A corresponds to the a axis, whereas the value of C only constitutes an upper bound for the c axis. In the case of a triaxial droplet, the value of A gives a lower bound for the a axis, whereas the value of C gives a lower bound for the b axis and an upper bound for the c axis. In this section, we will discuss the experimental results in terms of the apparent A , C , and AR values, from which the average actual sizes of the axisymmetric droplets are obtained. The values of A and C are obtained from the diffraction patterns as described elsewhere (see supplemental material in Ref. [14]).

The values of the half axes A and C , as well as their AR s, are noted for each panel in Fig. 1. The calculated A and C values from Fig. 1(a) are very similar (within $\sim 3\%$), indicative of a spherical droplet shape or a spheroid with its symmetry axis aligned perpendicular to the detector plane. The diffraction pattern shown in Fig. 1(b) originates from a droplet with larger values of A and C . Here, the two half axes differ by $\sim 34\%$ ($AR = 1.34$), which is indicative of a spheroidal or ellipsoidal droplet. The streaked diffraction image in Fig. 1(c) corresponds to a strongly deformed, capsule-shaped droplet with $AR = 1.95$. The capsule shape is indicated by the small curvature of the streak, as discussed earlier [14,16]. All images in Fig. 1 exhibit blank horizontal stripes along their middle sections. These result from the gap between the upper and the lower panels of the pn CCD detector. Vertical stripes on the lower panel are caused by imperfect data readout for strong diffraction images.

During the measurements, approximately 900 intense diffraction images from pure ^3He droplets are obtained, each providing a unique set of A and C values. Similar measurements are performed for ^4He droplets, providing ~ 300 patterns as an independent reference for comparison. The measurements for a given isotopic fluid do not exhibit any systematic variation with nozzle temperature; thus, the results obtained at different temperatures are combined to improve statistics. Table S1 in the SM [36] lists the nozzle temperatures and corresponding numbers of recorded diffraction images for all experimental runs. Figure 2(a) displays the measured distribution of the droplet's major half axis, A , for ^3He and ^4He droplets, as represented by blue and red bars, respectively. The average value of A in ^4He droplets is approximately a factor of 2 larger than that of ^3He droplets. The values for the ^3He droplets vary between $A = 52$ nm and $A = 796$ nm, whereas ^4He droplets exhibit a larger spread, ranging from $A = 55$ nm to $A = 1250$ nm. Figure 2(b) shows the AR distribution for ^3He and ^4He droplets. The largest AR s are 1.99 for ^3He and 1.72 for ^4He . Figures 2(a) and 2(b) show that both the values of A and $(AR - 1)$ follow exponential distributions. Square symbols in panel (c) of Fig. 2 show the average aspect ratio for each of the bins in panel (a) for droplets with $AR < 1.4$, which correspond to oblate pseudospheroidal shapes as discussed in the following. The results of single measurements with $AR > 1.4$ in panel (c) are shown by stars. It is seen that in ^3He droplets, the average aspect ratio increases linearly from ~ 1.03 in small droplets with $A < 100$ nm to ~ 1.15 in larger droplets with $A \sim 600$ nm. Corresponding points for ^4He droplets also follow linear dependence with a somewhat smaller slope and have $\langle AR \rangle \sim 1.12$ at $A > 600$ nm. The AR distribution in each bin from Fig. 2(a) is found to be close to exponential. In contrast to the temperature-independent droplet sizes reported here, previous measurements on ^4He droplets found continuous increases in sizes with decreasing temperature [10]. At $T_0 < 4$ K and $P_0 = 20$ bars, ^4He expansion leads to the formation of a jet that breaks up into micron-sized droplets due to Rayleigh instability [10,40,41]. This mechanism gives rise to an extremely collimated beam of droplets, the occurrence of which was not observed during this work with either

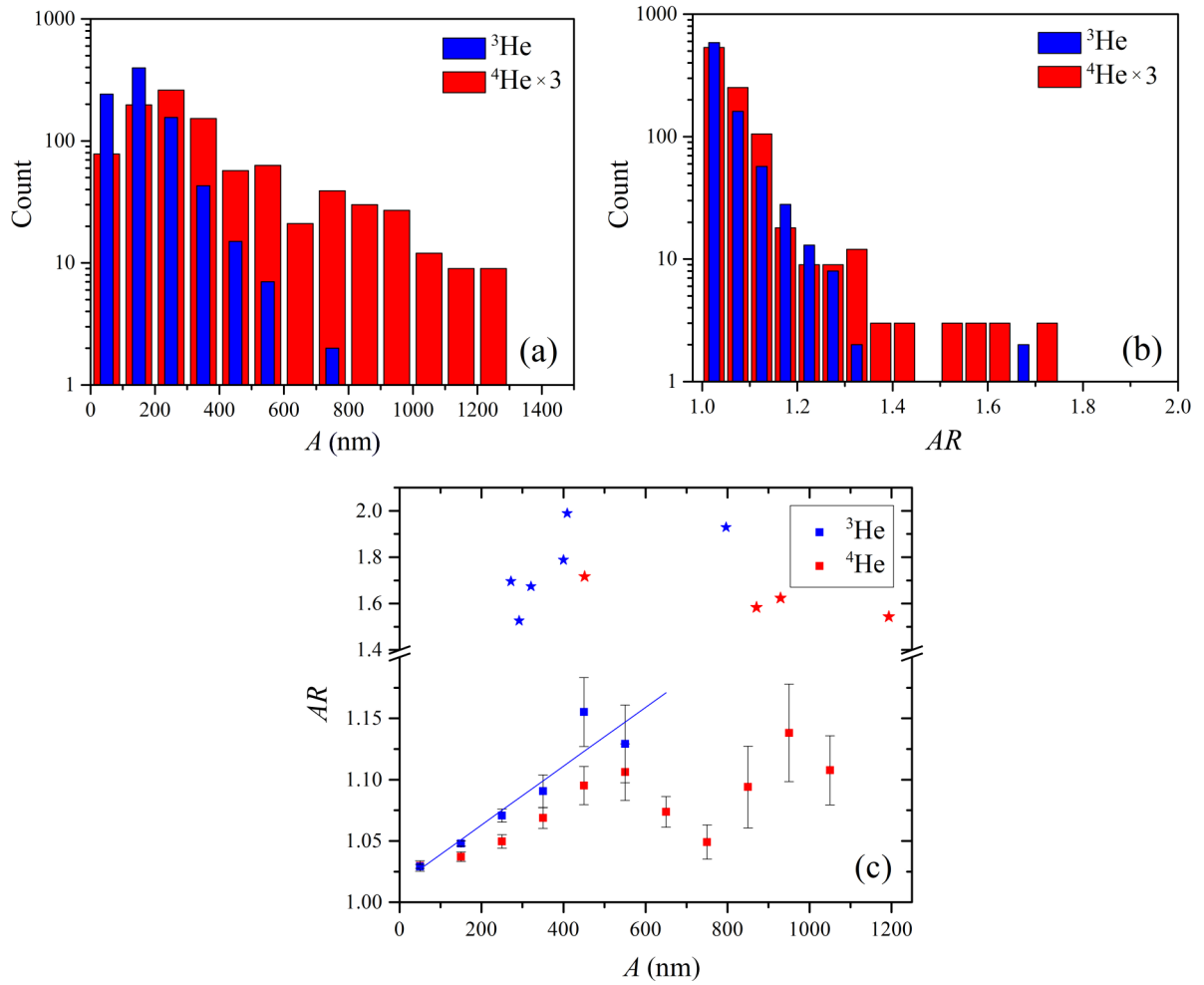


FIG. 2. Droplet size A (a) and aspect ratio AR (b) distributions for ^3He (blue) and ^4He (red) isotopes presented in logarithmic scales. The counts for ^4He were multiplied by a factor of 3 for ease of comparison, as the total number of diffraction images obtained for ^3He and ^4He were ~ 900 and ~ 300 , respectively (see Table S1 in SM [36]). Squares in panel (c) show average AR as obtained for each bin in panel (a) for the points with $AR < 1.4$. The results of single measurements with $AR > 1.4$ are shown by stars in panel (c). The blue line in panel (c) represents a linear fit of the data points (blue squares) for ^3He droplets.

^3He or ^4He . We conclude that, most likely, the flow through the nozzle in this work was affected by imperfections such as microscopic damage or partial obstruction by some solid impurities. Previous experiments with ^4He droplets in our group demonstrated that, under such conditions, decreasing the nozzle temperature below a certain value does not result in any increase in average droplet size [42], which is in agreement with the observations in this work.

IV. DISCUSSION

A. Droplet size distribution

From Fig. 2(a), we notice that the observed droplet size distributions peak at some small value of A , and decrease both toward larger and smaller A . The measured distribution reflects the actual distribution in the beam multiplied by the detection efficiency for a droplet of apparent half axis A in the diffraction experiment. In the SM [36], it is shown that for a spherical droplet, the detection efficiency scales as $\ln \frac{R^4}{R_0^4}$

for $R \geq R_0$ and it is zero for $R < R_0$, where R is the radius of the droplet and $R_0 \approx 50$ nm is the radius of the smallest detectable droplet. Accordingly, for $R \gg R_0$ the detection probability is a slowly changing logarithmic function of R . However, as R approaches R_0 , the detection efficiency goes to zero, which explains the decrease of the counts at small A in Fig. 2(a). In view of the approximate nature of the derivation, no corrections regarding the detection efficiency were applied in this work.

Droplet size distributions are usually discussed in terms of the number of atoms per droplet, owing to the detection technique, which is often based on mass spectroscopy [43]. For an oblate droplet the number of He atoms is given by $N = \frac{4\pi n a^2 c}{3}$, where n is the number density of liquid ^3He or ^4He at low temperature, with values of $1.62 \times 10^{28} \text{ m}^{-3}$ [32] and $2.18 \times 10^{28} \text{ m}^{-3}$ [44], respectively. Here, we approximate the true values of a and c for each droplet by the measured projection values of $A = a$ and $C \leq c$. Since, as discussed in the following section, the average aspect ratio of the droplets is close to unity, this approximation will overesti-

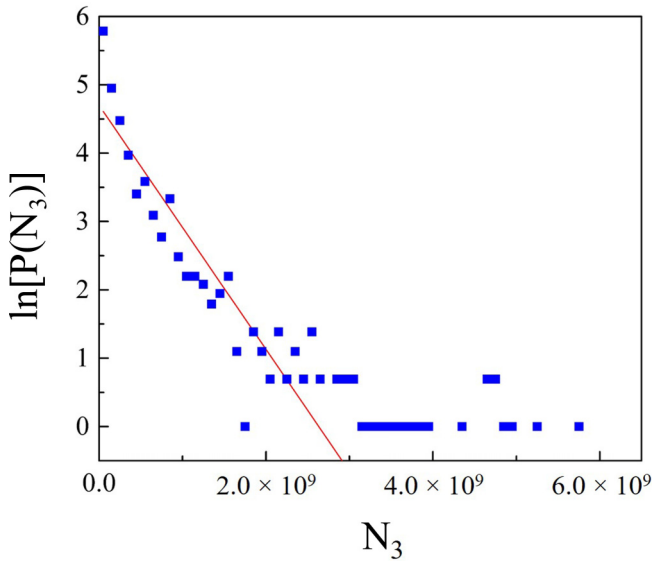


FIG. 3. Measured size distribution of ${}^3\text{He}$ droplets (blue squares). The red line represents $\ln(P) = 4.7 - N_3/\langle N_3 \rangle$ with $\langle N_3 \rangle = 5.6 \times 10^8$; see text for details. The figure does not include nine droplets in the range $N_3 = 7 \times 10^9 - 2 \times 10^{10}$, which are off scale.

mate the droplet number sizes by only a few percent, which is comparable to the statistical error. Accordingly, average number sizes for droplets with aspect ratios of less than 1.4 are $\langle N_3 \rangle = (5.6 \pm 0.1) \times 10^8$ and $\langle N_4 \rangle = (1.1 \pm 0.1) \times 10^{10}$. Figure 3 shows the number size distribution for ${}^3\text{He}$ droplets on a natural logarithmic scale. For comparison, the red line indicates an exponential distribution $P(N_3) = \frac{S}{\langle N_3 \rangle} \exp(-\frac{N_3}{\langle N_3 \rangle})$, with S being the total number of detected droplets. This approximation is in good agreement with the experimental data for sizes $N_3 \leq 3 \times 10^9$. An exponentially declining size distribution was also found in a recent study of ${}^4\text{He}$ droplets obtained from a pulsed nozzle at the FERMI FEL [16]. In comparison, the size distribution of smaller ${}^3\text{He}$ droplets with $N_3 \leq 10^7$ obtained at $P_0 = 20$ bar and $T_0 \geq 5$ K was found to be close to log-normal [37].

B. Droplet aspect ratios

The aspect ratios provide access to the angular momentum and angular velocity of the droplets. One can obtain the average actual aspect ratio $\langle ar \rangle$ from the average apparent aspect ratio $\langle AR \rangle$ assuming a random droplet orientation as described in the following.

In classical droplets, the largest aspect ratio of stable, axially symmetric droplets is $ar = 1.47$ [34,35]. About 99% of the measurements in Fig. 2 have $AR < 1.4$, in agreement with previous measurements in ${}^4\text{He}$ droplets [11,14–16]. Here, we assume that an overwhelming majority of droplets with $AR < 1.4$ have oblate, axially symmetric shapes. We also assume that the data set contains less than about ten events from prolate He droplets that are oriented in such a way that their projections yield $AR < 1.4$ and cannot be distinguished from oblate droplets. This estimate is based on the number of events producing $AR > 1.4$, which are entirely ascribed to prolate droplets. For more details, see Fig. 11 in Ref. [14] and the

corresponding text. For shapes with $AR < 1.4$, the average values for the observed major half axis A and aspect ratio AR are $\langle A_3 \rangle = 160 \pm 3$ nm, $\langle AR_3 \rangle = 1.049 \pm 0.003$, $\langle A_4 \rangle = 348 \pm 14$ nm, $\langle AR_4 \rangle = 1.059 \pm 0.005$, where the subscripts 3 and 4 refer to ${}^3\text{He}$ and ${}^4\text{He}$, respectively.

To translate the measured $\langle AR \rangle$ into the actual $\langle ar \rangle$, we assume a spheroid with a well-defined ar and calculate its projection on the detector plane when its symmetry axis c forms an angle α with the normal to the plane. The aspect ratios of the diffraction pattern (AR) and of the spheroid off which the x-rays diffract (ar) are related by $AR = \sqrt{\cos^2(\alpha) + ar^2 \sin^2(\alpha)}$ (see Eq. (S2.8) in the supplemental material of Ref. [11]). The average AR of an ensemble of randomly aligned droplets is then calculated as $\langle AR \rangle = \int_0^{\pi/2} AR(\alpha) \sin(\alpha) d\alpha$, where $\sin(\alpha)$ represents the probability of finding a spheroid at angle α . Integration and second-order expansion near $\langle AR \rangle = 1$ yields $\langle AR \rangle - 1 = \frac{2}{3}(ar - 1) + \frac{1}{15}(ar - 1)^2$. The expression is approximately linear within less than 5% error in the range of $1 \leq ar \leq 1.4$. Due to the linear relationship between $\langle AR \rangle$ and ar , the same formula also applies when considering not just an orientation-averaged ensemble with one specific ar , but also averages over all orientations; thus $\langle ar \rangle - 1 \approx \frac{3}{2}(\langle AR \rangle - 1)$. From this relationship, the average true aspect ratios for ${}^3\text{He}$ and ${}^4\text{He}$ droplets are derived as $\langle ar_3 \rangle = 1.074 \pm 0.005$ and $\langle ar_4 \rangle = 1.088 \pm 0.008$, respectively.

C. Average angular momenta and angular velocities of ${}^3\text{He}$ and ${}^4\text{He}$ droplets

As previously described for ${}^4\text{He}$ droplets [11,14–17], we ascribe the shape deformation in ${}^3\text{He}$ droplets to centrifugal distortion. It has been reported that the shapes of rotating ${}^4\text{He}$ droplets closely follow the equilibrium shapes of classical droplets having the same values of angular momentum [14,16,17,20,21]. This pattern is also expected to be the case of ${}^3\text{He}$ droplets, which at the temperature of these experiments (~ 0.15 K) [29] should behave classically due to the high viscosity of about 200 μP and small mean free path (a few nanometers) of elementary excitations at this temperature [32]. In recent density functional calculations, the shapes of rotating ${}^3\text{He}$ droplets were found to be very close to those predicted for classical droplets [33]. The blue curves in Figure 4 show the stability diagram of the classical droplets in terms of the reduced angular momentum (Λ) and reduced angular velocity (Ω), which are given by [34,35]

$$\Lambda = \frac{L}{\sqrt{8\sigma\rho R^7}}, \quad (1)$$

$$\Omega = \sqrt{\frac{\rho R^3}{8\sigma}} \omega. \quad (2)$$

Here, L and ω are the angular momentum and angular velocity, respectively; σ is the surface tension of the liquid; ρ is the liquid mass density, and R is the droplet radius in a quiescent state. For liquid ${}^4\text{He}$ and ${}^3\text{He}$ at low temperature, the surface tensions are $\sigma_4 = 3.54 \times 10^{-4}$ N/m [44] and $\sigma_3 = 1.55 \times 10^{-4}$ N/m [45], respectively, while their densities are $\rho_4 = 145$ kg/m³ [44] and $\rho_3 = 82$ kg/m³ [32]. With increasing Λ , the droplet's equilibrium shape transitions from

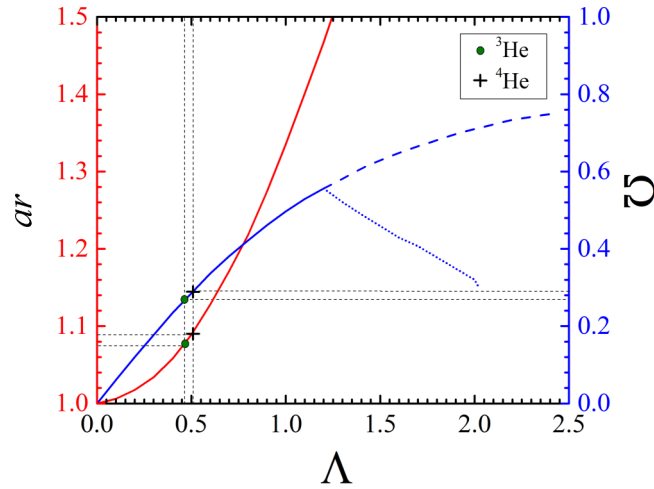


FIG. 4. Red curve: Calculated aspect ratio ar as a function of reduced angular momentum (Λ) for axially symmetric oblate droplet shapes. Blue curve: stability diagram of rotating droplets in terms of reduced angular velocity (Ω) and reduced angular momentum (Λ). The upper branch (dashed blue) corresponds to unstable axially symmetric shapes. The lower branch (dotted blue) is associated with prolate triaxial droplet shapes resembling capsules and dumbbells. The green circle and black cross on the red curve represent the average $\langle ar \rangle$ for ${}^3\text{He}$ and ${}^4\text{He}$ droplets, respectively, obtained in this work (with $AR < 1.4$). Similar markers on the blue curve indicate the (Ω, Λ) values corresponding to ${}^3\text{He}$ and ${}^4\text{He}$ droplets.

spherical to oblate axially symmetric, which is shown by the solid blue curve. At $\Omega \approx 0.56$, $\Lambda \approx 1.2$, $ar \approx 1.47$, the stability curve bifurcates into two branches: an unstable upper branch (dashed blue curve) representing axially symmetric droplets and a stable lower branch (dotted blue curve) representing prolate triaxial droplets. The stable prolate branch represents triaxial ellipsoidal and capsule-shaped droplets with $1.2 < \Lambda < 1.6$, and dumbbell-shaped droplets at $\Lambda > 1.6$ [14,16,34,35]. For $\Lambda > 2$, droplets become unstable and break up. Also shown in Fig. 4 is the ar of droplets along the axisymmetric branch as a function of Λ , which is represented by the red curve [14]. Using an exponential distribution of the ar values, $P(ar - 1) = \frac{1}{\langle ar - 1 \rangle} \exp(-\frac{ar-1}{\langle ar-1 \rangle})$, (see Fig. 2b) and the functions of $\Lambda(ar)$ and $\Omega(ar)$ in Fig. 4, integration over ar gives the average Λ and Ω for ${}^3\text{He}$ and ${}^4\text{He}$ droplets to be $\langle \Lambda_3 \rangle = 0.47$, $\langle \Omega_3 \rangle = 0.27$ and $\langle \Lambda_4 \rangle = 0.51$, $\langle \Omega_4 \rangle = 0.29$. Those values are indicated in Fig. 4 as green circles and black crosses, respectively. Very similar values were obtained for ${}^3\text{He}$ by integrating a double exponential distribution of the form

$$P(ar - 1, A) = \frac{1}{\langle ar(A) - 1 \rangle} \exp(-\frac{ar-1}{\langle ar(A) - 1 \rangle}) \frac{1}{\langle A \rangle} \exp(-\frac{A}{\langle A \rangle})$$

where the values of $ar(A)$ were obtained from the blue line in Fig. 2(c) multiplied by 1.5 (see section IV B). Although the values of $\langle AR \rangle$ versus A in Fig. 2(c) lie somewhat lower for ${}^4\text{He}$ than for ${}^3\text{He}$, the corresponding average values for ${}^4\text{He}$ are larger due to a larger prevalence of large ${}^4\text{He}$ droplets. From the values of $\langle \Lambda_{3,4} \rangle$ and $\langle \Omega_{3,4} \rangle$ and using Eqs. (1) and (2), the angular momentum (L) is obtained as $L_3 = 1.5 \times 10^9 \hbar$ and $L_4 = 6.9 \times 10^{10} \hbar$ for the average-sized ${}^3\text{He}$ and ${}^4\text{He}$ droplets, respectively. Next, L per atom of the droplet is obtained as $5.7\hbar$ and $19.3\hbar$ for ${}^3\text{He}$

and ${}^4\text{He}$ droplets, respectively. Lastly, ω was calculated as 1.6×10^7 and 5.9×10^6 rad/s for ${}^3\text{He}$ and ${}^4\text{He}$, respectively. Although the ${}^4\text{He}$ droplets and ${}^3\text{He}$ droplets have similar $\langle \Lambda \rangle$, ${}^4\text{He}$ droplets have about a factor of 3 larger L per atom. Mathematically, this effect stems from the different factors of $\sqrt{\sigma \rho R^7}$ in Eq. (1) in ${}^3\text{He}$ and ${}^4\text{He}$ droplets.

D. Formation of rotating droplets in the fluid jet expansion

It is remarkable that despite their very different physical properties, ${}^3\text{He}$ and ${}^4\text{He}$ droplets have very similar values of Ω and Λ on average. Previous XFEL experiments with ${}^4\text{He}$ droplets yielded average aspect ratios, $\langle AR \rangle$, in the range of 1.06 – 1.08 at $P_0 = 20$ bar and $T_0 = 4 - 7$ K, which spans average droplet sizes from 200 to 1000 nm in diameter (see Fig. 4.11 in Ref. [42]). Thus, it is noteworthy that very similar average aspect ratios, and therefore Ω and Λ , were obtained at a different T_0 . Comparable $\langle AR \rangle$ were obtained in experiments involving different nozzle plates, including measurements with partially obstructed and intact nozzles [42]. Hence, it seems that the acquired $\langle AR \rangle$ is largely independent of particular nozzles used in the experiments. Similar results for nonsuperfluid ${}^3\text{He}$ and superfluid ${}^4\text{He}$ droplets indicate that the state of the droplets has a small effect on the resulting average reduced angular momentum.

In previous works [14,46], we conjectured that during the passage of fluid helium through the nozzle, the fluid interacts with the nozzle channel walls and acquires vorticity, which is eventually transferred to the droplets. Accordingly, the estimated average angular velocity of ${}^4\text{He}$ and ${}^3\text{He}$ droplets is 3.4×10^7 and 4.5×10^7 rad/s, respectively. Such high angular velocities can only be sustained by rather small droplets.

It is challenging to explain the similarities in reduced angular velocity and angular momentum in ${}^3\text{He}$ and ${}^4\text{He}$ droplets based on the stability diagram in Fig. 4 and the estimated vorticities. Moreover, the half axis and shape distributions in Fig. 2, as observed at high vacuum far downstream (~ 70 cm) from the nozzle, originate from processes in the high-density region inside or close to the nozzle, where collisions between droplets with the dense He gas must play an important role. For example, for a droplet with a radius of 300 nm, rotating at 10^7 rad/s, the peripheral velocity will be ~ 3 m/s, assuming rigid body rotation. In the regime of extensive jet atomization as in this work, a large spread of droplet velocities up to $\Delta v/v \sim 5\%$ has previously been observed [47]. Thus, with a characteristic droplet velocity on the order of 200 m/s, the droplets may have significant relative collision velocities of ~ 10 m/s, which are sufficient to produce rapidly spinning products. Further downstream, presumably a few millimeters away from the nozzle, the number density of the gas and droplets decreases, the collision rates decrease, and the angular momenta of individual droplets remain constant further downstream.

Although we are currently unable to provide a quantitative model of the processes close to the nozzle, it is instructive to consider the evolution of a droplet driven at some angular velocity as opposed to free droplets with a constant angular momentum. The corresponding driving force may originate from the aforementioned collisions. The prolate branch on the stability curve of driven droplets is unstable at constant ω

[34]. Driven droplets will climb along the axially symmetric branch until they reach the bifurcation point at $\Omega = 0.56$ (Fig. 4) at which point they will enter the unstable prolate branch. Here, further elongation of the droplets occurs, culminating in their fission. The stable configurations beyond the fission point correspond to two spherical droplets, each having one half the volume of the parent droplet [34]. On the other hand, scission of dumbbell-shaped droplets will result in strongly deformed fragments. Related theoretical studies of nuclear fission indicate that such fragments contain sizable angular momentum [48,49]. Similar to the parent droplets, daughter droplets will acquire angular momentum via collisions. The fission cycle continues until sufficiently small, stable droplets are formed or the droplets are far away from the nozzle, where the driving force diminishes. Because the occurrence of such a cycle is largely independent of the He isotope, the process should yield very similar values of $\langle AR \rangle$, $\langle \Lambda \rangle$, and $\langle \Omega \rangle$, independent of the droplet size and composition. This model is also consistent with the trend apparent in Fig. 2(c) that larger droplets exhibit larger values of $\langle AR \rangle$.

V. CONCLUSIONS

In this work, bosonic ^4He and fermionic ^3He droplets are studied by single-pulse x-ray coherent diffractive imaging. Statistics of the droplets' sizes, aspect ratios, reduced angular momenta, and reduced angular velocities are compared for superfluid ^4He droplets and normal fluid ^3He droplets. Since the experiments only give access to projections of droplets onto the detector plane, estimates are made to determine the true average axis lengths and aspect ratios. It is found that, although superfluid droplets have a much higher average angular momentum, the two kinds of droplets have very similar average aspect ratios and, thus, similar average reduced angular momenta and reduced angular velocities. This observation may result from the formation of the droplets through turbulent nozzle flow and the atomization regime in the immediate vicinity of the nozzle. We conjecture that the droplets' rotation is driven by a combination of the liquid flow velocity gradient inside the nozzle and collisions close

to it, leading to elongation and, ultimately, fragmentation into daughter droplets, which may undergo repeated collision-elongation-fragmentation cycles.

Future studies will shed more light on the origin of angular momentum in droplets produced via fluid fragmentation. A large number of studies discuss the fragmentation of classical liquids upon jet expansion [50,51]. However, not much is known about the amount of angular momentum contained in the resulting droplets. It is therefore interesting to see that the jet atomization of classical liquids produces highly rotating droplets similar to He quantum droplets.

The availability of the large ^3He droplets suitable for single-pulse diffraction experiments also opens additional research directions. Vortex-induced cluster aggregation has so far been unique to superfluid ^4He . It is of high interest to expand diffraction experiments to nonsuperfluid ^3He and study the aggregation patterns in rotating fermionic droplets. Dopant aggregation mechanisms and the morphology of the phase separation in rotating mixed $^3\text{He}/^4\text{He}$ droplets present another frontier [52].

ACKNOWLEDGMENTS

This material is based upon work supported by the National Science Foundation under Grant No. DMR-1701077 (A.F.V.). C.A.S., B.W.T., M.B., and O.G. are supported by the US Department of Energy, Office of Science, Office of Basic Energy Sciences, Chemical Sciences, Geosciences and Biosciences Division, through Contract No. DE-AC02-05CH11231. M.B. acknowledges support by the Alexander von Humboldt foundation. Portions of this research were carried out at the Linac Coherent Light Source (LCLS) at the SLAC National Accelerator Laboratory, a user facility operated by Stanford University on behalf of the US DOE, OBES, under beamtime Grant No. LU46: Molecular Self-Assembly Close to 0 Kelvin. Use of LCLS is supported by the US Department of Energy, Office of Science, Office of Basic Energy Sciences, under Contract No. DE-AC02-76SF00515. We thank Manuel Barranco for carefully reading the manuscript and making Ref. [33] available to us prior to publication.

-
- [1] J. P. Toennies and A. F. Vilesov, Superfluid helium droplets: A uniquely cold nanomatrix for molecules and molecular complexes, *Angew. Chem., Int. Ed.* **43**, 2622 (2004).
 - [2] M. Y. Choi, G. E. Douberly, T. M. Falconer, W. K. Lewis, C. M. Lindsay, J. M. Merritt, P. L. Stiles, and R. E. Miller, Infrared spectroscopy of helium nanodroplets: Novel methods for physics and chemistry, *Int. Rev. Phys. Chem.* **25**, 15 (2006).
 - [3] M. Barranco, R. Guardiola, S. Hernandez, R. Mayol, J. Navarro, and M. Pi, Helium nanodroplets: An overview, *J. Low Temp. Phys.* **142**, 1 (2006).
 - [4] R. M. P. Tanyag, C. F. Jones, C. Bernando, S. M. O. O'Connell, D. Verma, and A. F. Vilesov, in *Cold Chemistry: Molecular Scattering and Reactivity Near Absolute Zero*, edited by O. Dulieu and A. Osterwalder (Royal Society of Chemistry, Cambridge, 2017), p. 389.
 - [5] D. Verma, R. M. P. Tanyag, S. M. O. O'Connell, and A. F. Vilesov, Infrared spectroscopy in superfluid helium droplets, *Adv. Phys.* **X 4**, 1553569 (2019).
 - [6] A. Mauracher, O. Echt, A. M. Ellis, S. Yang, D. K. Bohme, J. Postler, A. Kaiser, S. Denifl, and P. Scheier, Cold physics and chemistry: Collisions, ionization and reactions inside helium nanodroplets close to zero K, *Phys. Rep.* **751**, 1 (2018).
 - [7] S. Grebenev, J. P. Toennies, and A. F. Vilesov, Superfluidity within a small helium-4 cluster: The microscopic Andronikashvili experiment, *Science* **279**, 2083 (1998).
 - [8] A. R. W. McKellar, Y. J. Xu, and W. Jager, Spectroscopic Exploration of Atomic Scale Superfluidity in Doped Helium Nanoclusters, *Phys. Rev. Lett.* **97**, 183401 (2006).

- [9] M. Lemeshko and R. Schmidt, in *Cold Chemistry: Molecular Scattering and Reactivity Near Absolute Zero*, edited by O. Dulieu and A. Osterwalder (Royal Society of Chemistry, Cambridge, 2017), p. 444.
- [10] L. F. Gomez, E. Loginov, R. Sliter, and A. F. Vilesov, Sizes of large He droplets, *J. Chem. Phys.* **135**, 154201 (2011).
- [11] L. F. Gomez, K. R. Ferguson, J. P. Cryan, C. Bacellar, R. M. P. Tanyag, C. Jones, S. Schorb, D. Anielski, A. Belkacem, C. Bernando, R. Boll, J. Bozek, S. Carron, G. Chen, T. Delmas, L. Englert, S. W. Epp, B. Erk, L. Foucar, and R. Hartmann *et al.*, Shapes and vorticities of superfluid helium nanodroplets, *Science* **345**, 906 (2014).
- [12] R. M. P. Tanyag, C. Bernando, C. F. Jones, C. Bacellar, K. R. Ferguson, D. Anielski, R. Boll, S. Carron, J. P. Cryan, L. Englert, S. W. Epp, B. Erk, L. Foucar, L. F. Gomez, R. Hartmann, D. M. Neumark, D. Rolles, B. Rudek, A. Rudenko, and K. R. Siefertmann *et al.*, Communication: X-ray coherent diffractive imaging by immersion in nanodroplets, *Struct. Dyn.* **2**, 051102 (2015).
- [13] C. F. Jones, C. Bernando, R. M. P. Tanyag, C. Bacellar, K. R. Ferguson, L. F. Gomez, D. Anielski, A. Belkacem, R. Boll, J. Bozek, S. Carron, J. Cryan, L. Englert, S. W. Epp, B. Erk, L. Foucar, R. Hartmann, D. M. Neumark, D. Rolles, and A. Rudenko *et al.*, Coupled motion of Xe clusters and quantum vortices in He nanodroplets, *Phys. Rev. B* **93**, 180510(R) (2016).
- [14] C. Bernando, R. M. P. Tanyag, C. Jones, C. Bacellar, M. Bucher, K. R. Ferguson, D. Rupp, M. P. Ziemkiewicz, L. F. Gomez, A. S. Chatterley, T. Gorkhover, M. Muller, J. Bozek, S. Carron, J. Kwok, S. L. Butler, T. Moller, C. Bostedt, O. Gessner, and A. F. Vilesov, Shapes of rotating superfluid helium nanodroplets, *Phys. Rev. B* **95**, 064510 (2017).
- [15] D. Rupp, N. Monserud, B. Langbehn, M. Sauppe, J. Zimmermann, Y. Ovcharenko, T. Moller, F. Frassetto, L. Poletto, A. Trabatttoni, F. Calegari, M. Nisoli, K. Sander, C. Peltz, M. J. Vrakking, T. Fennel, and A. Rouzee, Coherent diffractive imaging of single helium nanodroplets with a high harmonic generation source, *Nat. Commun.* **8**, 493 (2017).
- [16] B. Langbehn, K. Sander, Y. Ovcharenko, C. Peltz, A. Clark, M. Coreno, R. Cucini, M. Drabbels, P. Finetti, M. Di Fraia, L. Giannessi, C. Grazioli, D. Iablonskyi, A. C. LaForge, T. Nishiyama, V. O. A. de Lara, P. Piseri, O. Plekan, K. Ueda, and J. Zimmermann *et al.*, Three-Dimensional Shapes of Spinning Helium Nanodroplets, *Phys. Rev. Lett.* **121**, 255301 (2018).
- [17] S. M. O. O'Connell, R. M. P. Tanyag, D. Verma, C. Bernando, W. Pang, C. Bacellar, C. A. Saladrigas, J. Mahl, B. W. Toulson, W. Kumagai, P. Walter, F. Ancilotto, M. Barranco, M. Pi, C. Bostedt, O. Gessner, and A. F. Vilesov, Angular Momentum in Rotating Superfluid Droplets, *Phys. Rev. Lett.* **124**, 215301 (2020).
- [18] K. Lehman and R. Schmied, Energetics and possible formation and decay mechanisms of vortices in helium nanodroplets, *Phys. Rev. B* **68**, 224520 (2003).
- [19] O. Gessner and A. Vilesov, Imaging quantum vortices in superfluid helium droplets, *Ann. Rev. Phys. Chem.* **70**, 173 (2019).
- [20] F. Ancilotto, M. Barranco, and M. Pi, Spinning superfluid He-4 nanodroplets, *Phys. Rev. B* **97**, 184515 (2018).
- [21] F. Ancilotto, M. Pi, and M. Barranco, Vortex arrays in nanoscopic superfluid helium droplets, *Phys. Rev. B* **91**, 100503 (2015).
- [22] J. Gspann and H. Vollmar, Metastable excitations of large clusters of ^3He , ^4He or Ne atoms, *J. Chem. Phys.* **73**, 1657 (1980).
- [23] P. W. Stephens and J. G. King, Experimental Investigation of Small Helium Clusters—Magic Numbers and the Onset of Condensation, *Phys. Rev. Lett.* **51**, 1538 (1983).
- [24] K. von Haeften, A. R. B. de Castro, M. Joppien, L. Moussavizadeh, R. von Pietrowski, and T. Möller, Discrete Visible Luminescence of Helium Atoms and Molecules Desorbing from Helium Clusters: The Role of Electronic, Vibrational, and Rotational Energy Transfer, *Phys. Rev. Lett.* **78**, 4371 (1997).
- [25] M. Farnik, U. Henne, B. Samelin, and J. P. Toennies, Differences in the Detachment of Electron Bubbles from Superfluid ^4He Droplets versus Nonsuperfluid ^3He Droplets, *Phys. Rev. Lett.* **81**, 3892 (1998).
- [26] J. Harms, M. Hartmann, B. Sartakov, J. P. Toennies, and A. F. Vilesov, High resolution infrared spectroscopy of single SF₆ molecules in helium droplets. II. The effect of small amounts of ^4He in large ^3He droplets, *J. Chem. Phys.* **110**, 5124 (1999).
- [27] J. Harms, J. P. Toennies, M. Barranco, and M. Pi, Experimental and theoretical study of the radial density distributions of large ^3He droplets, *Phys. Rev. B* **63**, 184513 (2001).
- [28] F. Stienkemeier, O. Bunermann, R. Mayol, F. Ancilotto, M. Barranco, and M. Pi, Surface location of sodium atoms attached to ^3He nanodroplets, *Phys. Rev. B* **70**, 214509 (2004).
- [29] B. G. Sartakov, J. P. Toennies, and A. F. Vilesov, Infrared spectroscopy of carbonyl sulfide inside a pure ^3He droplet, *J. Chem. Phys.* **136**, 134316 (2012).
- [30] S. Grebenev, B. G. Sartakov, J. P. Toennies, and A. F. Vilesov, The structure of the OCS-H₂ van der Waals complex embedded inside $^4\text{He}/^3\text{He}$ droplets, *J. Chem. Phys.* **114**, 617 (2001).
- [31] D. R. Tilley and J. Tilley, *Superfluidity and Superconductivity* (Institute of Physics Publishing, Bristol, UK, 1990).
- [32] E. R. Dobbs, *Helium Three* (Oxford University Press, New York, 2000).
- [33] M. Pi, F. Ancilotto, and M. Barranco, Rotating He droplets, *J. Chem. Phys.* **152**, 184111 (2020).
- [34] R. A. Brown and L. E. Scriven, The shape and stability of rotating liquid-drops, *Proc R. Soc. London, Ser. A* **371**, 331 (1980).
- [35] S. L. Butler, M. R. Stauffer, G. Sinha, A. Lilly, and R. J. Spiteri, The shape distribution of splash-form tektites predicted by numerical simulations of rotating fluid drops, *J. Fluid Mech.* **667**, 358 (2011).
- [36] See Supplemental Material at <http://link.aps.org/supplemental/10.1103/PhysRevB.102.014504> for more information on $^3\text{He}/^4\text{He}$ P-T diagrams, detection probability of He droplets, list of experimental runs, and the ^3He recycling system.
- [37] B. Samelin, Lebensdauer und neutralisation metastabiler, negative geladener Helium-Mikrotropfen, Ph.D. thesis, University of Göttingen, 1998.
- [38] L. Struder, S. Eppa, D. Rolles, R. Hartmann, P. Holl, G. Lutz, H. Soltau, R. Eckart, C. Reich, K. Heinzinger, C. Thamm, A. Rudenko, F. Krasniqi, K. U. Kuhnel, C. Bauer, C. D. Schroter, R. Moshhammer, S. Techert, D. Miessner, and M. Porro *et al.*, Large-format, high-speed, X-ray pnCCDs combined with electron and ion imaging spectrometers in a multipurpose chamber for experiments at 4th generation light sources, *Nucl. Instrum. Methods Phys. Res., Sect. A* **614**, 483 (2010).

- [39] K. R. Ferguson, M. Bucher, J. D. Bozek, S. Carron, J. C. Castagna, R. Coffee, G. I. Curiel, M. Holmes, J. Krzywinski, M. Messerschmidt, M. Minitti, A. Mitra, S. Moeller, P. Noonan, T. Osipov, S. Schorb, M. Swiggers, A. Wallace, J. Yin, and C. Bostedt, The atomic, molecular and optical science instrument at the linac coherent light source, *J. Synchrotron Radiat.* **22**, 492 (2015).
- [40] M. Kühnel, N. Petridis, D. F. A. Winters, U. Popp, R. Dörner, Th. Stöhlker, and R. E. Grisenti, Low-Z internal target from a cryogenically cooled liquid microjet source, *Nucl Instrum. Methods Phys. Res.* **602**, 311 (2009).
- [41] R. M. P. Tanyag, A. J. Feinberg, S. M. O. O'Connell, and A. F. Vilesov, Disintegration of diminutive liquid helium jets in vacuum, *J. Chem. Phys.* **152**, 234306 (2020).
- [42] R. M. P. Tanyag, Imaging superfluid helium droplets, Ph.D. thesis, University of Southern California, 2018.
- [43] U. Henne and J. P. Toennies, Electron capture by large helium droplets, *J. Chem. Phys.* **108**, 9327 (1998).
- [44] R. J. Donnelly and C. F. Barenghi, The observed properties of liquid helium at the saturated vapor pressure, *J. Phys. Chem. Ref. Data* **27**, 1217 (1998).
- [45] M. Iino, M. Suzuki, A. J. Ikushima, and Y. Okuda, Surface tension of liquid ^3He down to 0.3 K, *J. Low Temp. Phys.* **59**, 291 (1985).
- [46] L. F. Gomez, E. Loginov, and A. F. Vilesov, Traces of Vortices in Superfluid Helium Droplets, *Phys. Rev. Lett.* **108**, 155302 (2012).
- [47] R. E. Grisenti and J. P. Toennies, Cryogenic Microjet Source for Orthotropic Beams of Ultralarge Superfluid Helium Droplets, *Phys. Rev. Lett.* **90**, 234501 (2003).
- [48] G. F. Bertsch, T. Kawano, and L. M. Robledo, Angular momentum of fission fragments, *Phys. Rev. C* **99**, 034603 (2019).
- [49] L. Bonneau, P. Quentin, and I. N. Mikhailov, Scission configurations and their implication in fission-fragment angular momenta, *Phys. Rev. C* **75**, 064313 (2007).
- [50] C. Dumouchel, On the experimental investigation on primary atomization of liquid streams, *Exp. Fluids* **45**, 371 (2008).
- [51] J. Eggers and E. Villermaux, Physics of liquid jets, *Rep. Prog. Phys.* **71**, 036601 (2008).
- [52] M. Barranco, M. Guilleumas, D. M. Jezek, R. J. Lombard, J. Navarro, and M. Pi, Nucleation in dilute ^3He - ^4He liquid mixtures at low temperatures, *J. Low Temp. Phys.* **117**, 81 (1999).